Spontaneous flow in active nematics: Effects induced by annular confinement

A. Aramini
Dipartimento di Matematica e Fisica "E. De Giorgi", Università del Salento, Lecce, Italy

G. Napoli*
Dipartimento di Matematica e Applicazioni "R. Caccioppoli", Università degli Studi di Napoli "Federico II", Napoli, Italy

S. Turzi
Dipartimento di Matematica, Politecnico di Milano, Milano, Italy

(Received 12 March 2025; accepted 10 July 2025; published 1 August 2025)

Within the framework of continuum mechanics for materials with relaxation, this study investigates activity-induced laminar flow in an active nematic confined within an annular domain. Subsequent to the formulation of the problem as a nonlinear boundary value problem, a bifurcation analysis of the governing equation demonstrates that the critical threshold for the initiation of spontaneous flow is dependent on the aspect ratio (thickness-to-radius) of the domain. The influence of domain curvature is twofold: firstly, it facilitates the inception of spontaneous motion by reducing the critical threshold; secondly, it resolves the indeterminacy inherent in the planar geometry, wherein, at an equivalent critical threshold, two distinct flow configurations may manifest: a unidirectional flow or a configuration exhibiting two counter-propagating bands. In the annular geometry, the double-band configuration, characterized by a thicker inner layer, exhibits the lowest activation threshold. With an augmentation of either activity or curvature, the principal motion transitions towards a predominantly unidirectional flow, accompanied by a narrow counter-rotating band adjacent to the outer boundary, aligning with experimental observations of confined bacterial colonies.

DOI: 10.1103/5vj2-5rg7

I. INTRODUCTION

Active systems, composed of self-driven units that continuously convert energy from their surroundings into directed motion, represent a paradigm in contemporary physics for modeling biological phenomena, such as the dynamics of cytoskeleton filaments, dense bacterial suspensions, and the collective motion of animal groups like bird flocks and fish schools [1–6].

Continuum models for single-component suspensions of rodlike objects offer a framework for describing active matter. These models build upon the Ericksen-Leslie theory for passive nematic liquid crystals [7] by incorporating active stress terms to account for the inherent activity of the constituent particles. Among these models, the Simha-Ramaswamy model [8] stands out for its simplicity, postulating a direct proportionality between the active stress and the nematic ordering tensor, $\mathbf{Q}$. The strength of the activity is governed by a parameter, ζ, with positive values corresponding to extensile behavior and negative values to contractile behavior. This model has successfully predicted various notable phenomena observed in active matter, including spontaneous flow [9,10], motility-induced phase separation [11,12], and the spontaneous division of active nematic droplets [13,14].

More recently, Turzi [15,16] developed a thermodynamically consistent theory of active nematic gels that incorporates viscoelasticity and introduces activity as a remodeling force. This eliminates the need to add an active stress term to the model. The active remodeling force competes with the natural relaxation process of the passive system and drives it out of equilibrium.

However, even for this simple channel geometry, different models apparently predict different flow profiles. For example, the analysis in [2,9,10,17] predicts only one bifurcation mode in the transition. In particular, when an active gel is confined between two channel walls and the velocity vanishes on both walls, no net flow of particles is observed, but only a shear flow with the formation of bands flowing in opposite directions. In contrast, other analytical and numerical studies [15,18–20] on similar equations show that spontaneous flow in a single direction and banding are possible at the same critical value of the activity. Therefore, the flow transition seems to have two equivalent modes, a condition we refer to as "two-fold degeneracy" of the bifurcation.

Recently, Marzorati and Turzi [21] employed equivariant bifurcation analysis to investigate spontaneous flow and its stability in confined active nematics between two parallel plates, considering various material parameters. Their analysis revealed that the bifurcation diagram consists of two coincident pitchfork bifurcations lying in orthogonal planes, resulting in four solution branches that intersect only at the origin. They showed that the two-fold mode degeneracy ob-

*Contact author: gaetano.napoli@unina.it

served in previous studies is essentially dictated by the system symmetry, so that it is robust against parameter changes and is not specific to any particular active matter model. This implies that two distinct modes of instability (typically spontaneous flow and banding) should be observed in active nematics, at the same critical value of the active parameter, contrary to the predictions of some earlier models.

In other words, breaking this degeneracy requires breaking the K_4 symmetry of the system. One possible way to achieve this is to study active flows in curved channels [4,5,22–27]. To this aim, we consider the spontaneous flow of active nematics in an annular geometry, where the curvature of the channel provides the necessary symmetry-breaking mechanism. Specifically, we investigate spontaneous flow in an active nematic gel confined within an annular domain, focusing on the influence of the channel aspect ratio (thickness over radius) on the onset of spontaneous motion and the resulting velocity profile.

In addition to its mathematical significance, this problem also has numerous physical and biological implications. Experiments are typically performed in enclosed channels. Furthermore, confining surfaces play a crucial role in the dynamics of biological active systems. For instance, confinement of bacterial colonies can facilitate the emergence of spontaneous laminar flow, transforming turbulent-like dynamics of bulk active fluids into self-organized coherent macroscopic flows that persist across length scales ranging from micrometers to meters and over timescales of hours. Interestingly, the transition from a turbulent to a coherently circulating state appears to be governed by the aspect ratio of the confining channel, rather than by an inherent length scale of the active fluid [28].

Motivated by the importance of the aspect ratio, we investigated spontaneous flow in an active nematic gel confined within an annular domain and studied how the annular slenderness influences the onset of spontaneous motion and the resulting velocity profile. Our findings reproduce certain characteristics observed in confined bacterial colonies studied experimentally [4,5,29]. Specifically, we find that for some activity strengths, the interplay between channel curvature, dipolar activity, and hydrodynamics induces a thin counter-rotating boundary layer near the outer boundary.

The paper is structured as follows. In Sec. II, we recall the model and the equations of motion. Section III focuses on specializing these equations to an annular domain, while in Sec. IV, we perform a linear bifurcation analysis to investigate the onset of spontaneous flow induced by activity. In particular, we examine the influence of the domain's aspect ratio on the critical threshold and the bifurcation modes. Section V extends our study through numerical simulations of the nonlinear equations, providing a discussion of the physical implications and key findings. Finally, we present our conclusions in Sec. VI and include an Appendix with detailed calculations for the derivation of the equations of motion.

II. MODEL

This section outlines the active nematic theory advanced by Turzi [15,16]. Contrary to traditional models that utilize the ordering tensor $\mathbf{Q}$ to represent uniaxial nematic symmetry, this approach employs a uniaxial, unit determinant *shape tensor* characteristic of nematic elastomer theory:

$$\mathbf{L}(\rho, \mathbf{n}) = a_0^2(\mathbf{n} \otimes \mathbf{n}) + \frac{1}{a_0}(\mathbf{I} - \mathbf{n} \otimes \mathbf{n}). \tag{1}$$

Here, $\mathbf{n}$ denotes the director field and a_0 is a shape parameter that measures the degree of alignment of molecules along $\mathbf{n}$. Although the shape parameter may exhibit a dependence on the density of the material, we choose to treat it as a constant in this specific context, in line with the assumption of incompressibility and spatially uniform density.

Building on the framework established in [15], the model incorporates two main components of the free energy density: the elastomeric free energy density per unit mass,

$$\sigma_{\mathrm{el}}(\mathbf{B}_{\mathrm{e}}, \mathbf{n}) = \frac{\mu}{2}[\mathrm{tr}(\mathbf{L}^{-1}\mathbf{B}_{\mathrm{e}} - \mathbf{I}) - \log\det(\mathbf{L}^{-1}\mathbf{B}_{\mathrm{e}})], \tag{2}$$

representing the energy costs associated with the deformation of the elastomeric network, where $\mathbf{B}_{\mathrm{e}}$ is the effective left-Cauchy-Green deformation tensor and μ the elastic modulus; and the Frank energy density

$$\sigma_{\mathrm{Fr}}(\nabla\mathbf{n}) = \frac{\kappa}{2}|\nabla\mathbf{n}|^2, \tag{3}$$

which captures the energy associated with the distortion of the nematic director field $\mathbf{n}$, with κ being the elastic modulus under the one-constant approximation. The fluidity of the material is taken into account by allowing the effective tensor $\mathbf{B}_{\mathrm{e}}$ to relax the internal stress according to the equation described below [see Eq. (6)].

Governing equations

Assuming no external forces and ignoring inertia effects, the balance of linear momentum simplifies to

$$\mathrm{div}\,\mathbf{T} = 0, \tag{4}$$

where the Cauchy stress tensor $\mathbf{T}$ is defined as

$$\mathbf{T} = -p\mathbf{I} + \rho\mu(\mathbf{L}^{-1}\mathbf{B}_{\mathrm{e}} - \mathbf{I}) - \rho\kappa(\nabla\mathbf{n})^{\top}(\nabla\mathbf{n}), \tag{5}$$

with p being the Lagrange multiplier associated with the incompressibility constraint $\det\mathbf{B}_{\mathrm{e}} = 1$.

A distinctive aspect of this theory, as noted in [15], is the absence of an explicit active component within the stress tensor $\mathbf{T}$. Instead, this theory accounts for stress dissipation, in agreement with irreversible thermodynamics, via an evolution equation for $\mathbf{B}_{\mathrm{e}}$

$$\mathbb{D}(\mathbf{B}_{\mathrm{e}}) + \rho\frac{\partial\sigma}{\partial\mathbf{B}_{\mathrm{e}}} = \mathbf{T}_a, \tag{6}$$

where $\mathbb{D}$ is a positive definite fourth-rank which contains the material relaxation timescales (see Ref. [30] for details); $\mathbf{B}_{\mathrm{e}}^{\nabla} := \dot{\mathbf{B}}_e - (\nabla\mathbf{v})\mathbf{B}_{\mathrm{e}} - \mathbf{B}_{\mathrm{e}}(\nabla\mathbf{v})^{\top}$ is the co-deformational derivative; and $\mathbf{T}_a$ the active tensor.

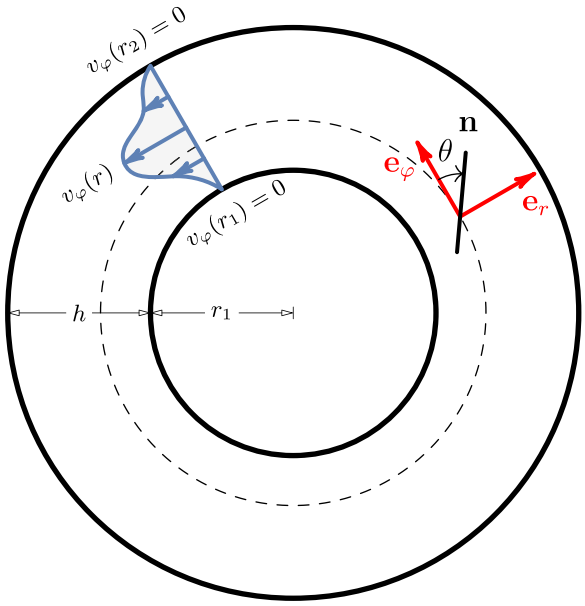

FIG. 1. Schematic representation of the channel geometry with no-slip conditions at walls $r = r_1$ and $r = r_2$, and planar boundary conditions for the nematic director. The diagram also illustrates our assumption of rotational invariance, indicating that all unknown fields depend solely on the transverse variable r, with the radial component of the velocity (v_r) assumed to be zero.

Finally, the director equation can be written as

$$\mathbf{n} \times \left[\rho \frac{\partial \sigma}{\partial \mathbf{n}} - \operatorname{div}\left(\rho \frac{\partial \sigma}{\partial \nabla \mathbf{n}} \right) \right] = \mathbf{0}, \tag{7}$$

where $\sigma = \sigma_{\text{el}} + \sigma_{\text{Fr}}$. After some algebra (see Appendix for calculation details), we find

$$\mathbf{n} \times \left[\mu \left(1 - a_0^{-3}\right) \mathbf{L}^{-1} \mathbf{B}_e \mathbf{n} + \kappa \Delta \mathbf{n} \right] = \mathbf{0}. \tag{8}$$

The problem involves two distinct timescales: τ_{def}, governed by macroscopic deformation (defined by $1/|\nabla \mathbf{v}|$), and τ_{rel} related to material remodeling and embedded within $\mathbb{D}$. When τ_{rel} is significantly shorter than τ_{def}, the material behaves effectively as a fluid, and we obtain a model for an active nematic fluid (see [15] for a comprehensive discussion). Under these conditions, with the additional assumptions,

$$\mathbf{T}_a = -\tfrac{1}{2} \rho \mu \zeta \mathbf{I}, \quad \mathbb{D} = \tfrac{1}{2} \rho \mu \tau \mathbb{I}, \tag{9}$$

where ζ is the dimensionless active coefficient and τ is a relaxation time, Eq. (5) simplifies to

$$\mathbf{T} = -p\mathbf{I} - \rho\mu(\tau \mathbf{L}^{\nabla} \mathbf{L} + \zeta \mathbf{L}) - \rho\kappa (\nabla \mathbf{n})^{\top} (\nabla \mathbf{n}). \tag{10}$$

It's important to note that the Cauchy stress tensor, Eq. (10), obtained under the fast relaxation approximation, contains an active term, specifically:

$$\mathbf{T}_{\text{active}} = -\rho \mu \zeta \mathbf{L}, \tag{11}$$

where the shape tensor $\mathbf{L}$ is given by Eq. (1). This active term can be compared to the classic formulation of active Cauchy stress [8,10,18], where $\mathbf{T}_{\text{active}} = -\bar{\zeta} \mathbf{Q}$, with $\mathbf{Q}$ being the nematic order tensor. Since both $\mathbf{Q}$ and $\mathbf{L}$ possess the same nematic symmetry, the two terms yield qualitatively analogous solutions.

Furthermore, the viscous components of the Cauchy stress – specifically, the second term in Eq. (10), which is $-\rho\mu\tau \mathbf{L}^{\nabla} \mathbf{L}$ – produces the standard Ericksen-Leslie stress tensor upon proper identification of the viscosity coefficients [30]. Within this model, the choice of a single relaxation time, τ, corresponds to establishing a particular relationship among the Leslie viscosity coefficients, as described in detail in [30]. It is worth noting that while classical theories might adopt alternative simplifications (for instance, considering only the Newtonian viscosity and the tumbling coefficient), different choices for these viscous coefficients generally do not alter the qualitative nature of the conclusions. In fact, the nature of the flow instabilities is mainly dictated by the underlying symmetry of the problem [21].

Finally, we note that the physical nature of the active term does not originate from jet-like propulsion generated by an internal chemical reaction, as studied, for example, in recent molecular simulations [25], but rather exhibits a dipolar character.

III. EQUATIONS OF MOTION IN AN ANNULAR RING

To explore the laminar flow of an active liquid crystal confined within a curved planar domain Ω, we detail the governing equations in polar planar coordinates. Specifically, the domain Ω is shaped as an annular ring, bounded by two concentric circles with radii r_1 and r_2 (see Fig. 1). The definition of Ω is given by:

$$\Omega := \{(r, \varphi) \in \mathbb{R}^2 \,:\, r_1 \leqslant r \leqslant r_2,\ 0 \leqslant \varphi < 2\pi\}. \tag{12}$$

Axial symmetry is assumed, with the fields dependent only on the radial coordinate r. To further simplify the analysis, we posit a purely azimuthal flow profile, characterized by a velocity field of the form $\mathbf{v} = v_\varphi(r)\mathbf{e}_\varphi$. Furthermore, we represent the director field $\mathbf{n}(r)$ in terms of the angle $\theta(r)$, which measures the deviation of $\mathbf{n}(r)$ from $\mathbf{e}_\varphi$, such that we write:

$$\mathbf{n} = \sin\theta(r)\mathbf{e}_r + \cos\theta(r)\mathbf{e}_\varphi. \tag{13}$$

In accordance with the no-slip boundary conditions, the azimuthal velocity is constrained to zero at both the inner and outer boundaries:

$$v_\varphi(r_1) = v_\varphi(r_2) = 0. \tag{14}$$

Additionally, we impose strong planar anchoring for the director field:

$$\theta(r_1) = \theta(r_2) = 0. \tag{15}$$

Given the aforementioned assumptions, Eq. (4) reduces to

$$T'_{rr} + r^{-1}(T_{rr} + T_{\varphi\varphi}) = 0, \tag{16a}$$

$$T'_{\varphi r} + r^{-1}(T_{\varphi r} - T_{r\varphi}) = 0. \tag{16b}$$

These equations, in conjunction with the explicit expressions for the stress tensor components $\mathbf{T}$, which are defined in terms of the fields p, v_φ, and θ, as detailed in

Appendix, yield:

$$2r^2\mu\rho\tau\cos(4\theta)\left(a_0^3-1\right)^2\theta'(v-rv')+2r^2\mu\rho\cos(2\theta)\left(2\zeta a_0\left(a_0^3-1\right)-\tau\left(a_0^6-1\right)\theta'(v-rv')\right)$$
$$+\frac{r}{2}\mu\rho\tau\sin(4\theta)\left(a_0^3-1\right)^2(v-r(v'+rv''))+r\mu\rho\sin(2\theta)\left(a_0^3-1\right)\left(3v\tau\left(a_0^3+1\right)+r\left(-3\tau\left(a_0^3+1\right)v'\right.\right.$$
$$\left.\left.-4r\zeta a_0\theta'+r\tau v''\left(a_0^3+1\right)\right)\right)-4a_0^2(r^3p'+\kappa\rho(-1+r^2\theta'(\theta'+2r\theta'')))=0, \tag{17a}$$

$$4\kappa a_0^2(\theta'+r\theta'')+4r\zeta\mu a_0\left(1-a_0^3\right)(\sin(2\theta)+r\theta'\cos(2\theta))-2\mu\tau\cos\theta(2\sin^2\theta(v-rv')(\cos\theta-4r\theta'\sin\theta)$$
$$+r^2v''\cos\theta(-3+\cos(2\theta)))-\mu\tau a_0^3((v-rv')(3+\cos(4\theta)-4r\theta'\sin(4\theta))-r^2v''(-1+\cos(4\theta)))$$
$$-2\mu\tau a_0^6\sin\theta(2\cos^2\theta(v-rv')(\sin\theta+4r\theta'\cos\theta)-r^2v''\sin\theta(3+\cos(2\theta)))=0. \tag{17b}$$

Furthermore, the director Eq. (7) can be expressed in terms of the fields v_φ and θ as follows:

$$v\mu\tau\left(\left(a_0^3-1\right)^2-\cos(2\theta)\left(a_0^6-1\right)\right)+rv'\mu\tau\left(a_0^3-1\right)\left(1+\cos(2\theta)-2a_0^3\sin^2\theta\right)+2\kappa a_0^2(\theta'+r\theta'')=0. \tag{18}$$

Equations (17) and (18) are to be considered in conjunction with the boundary conditions (14) and (15).

Dimensionless equations

Let us define the channel thickness $h := r_2 - r_1$ and the dimensionless radial variable

$$\xi := \frac{r-r_1}{h}, \quad 0 \leqslant \xi \leqslant 1. \tag{19}$$

Our problem has three characteristic lengths: h, r_1 and the intrinsic length ℓ defined by

$$\ell := \sqrt{\frac{\kappa}{\mu}}. \tag{20}$$

Hence, it is beneficial to introduce the dimensionless parameters

$$\alpha := \frac{h}{r_1}, \quad \eta := \frac{h}{\ell}, \tag{21}$$

which give the ratio of these lengths. The parameter α denotes the *aspect ratio* of the channel, and we will specifically analyze how both the solutions and the critical threshold are influenced by α. We also introduce the dimensionless functions $V(\xi)$ and $q(\xi)$ such that

$$v(r) = \frac{h}{\tau}V(\xi)\Big|_{\xi=(r-r_1)/h}, \tag{22a}$$

$$\theta(r) = q(\xi)|_{\xi=(r-r_1)/h}. \tag{22b}$$

Consequently, Eqs. (17b) and (18) are rewritten as

$$4\alpha a_0^2(\alpha\xi+1)q''+q'\left(4\alpha^2a_0^2-4a_0\left(a_0^3-1\right)\zeta\eta^2(\alpha\xi+1)^2\cos(2q)\right)-4\alpha a_0\left(a_0^3-1\right)\zeta\eta^2(\alpha\xi+1)\sin(2q)$$
$$+V'\left[8\eta^2\left(a_0^3-1\right)(\alpha\xi+1)^2q'\sin(2q)\left(a_0^3\cos^2q+\sin^2q\right)+\frac{1}{2}\alpha\eta^2(\alpha\xi+1)\left(-\left(a_0^3-1\right)^2\cos(4q)+a_0^6+6a_0^3+1\right)\right]$$
$$+V\left[-8\alpha\eta^2\left(a_0^3-1\right)(\alpha\xi+1)q'\sin(2q)\left(a_0^3\cos^2q+\sin^2q\right)-\alpha^2\eta^2\left(a_0^6\sin^2(2q)+a_0^3(\cos(4q)+3)+\sin^2(2q)\right)\right]$$
$$-\frac{1}{2}\eta^2(\alpha\xi+1)^2V''\left(\left(a_0^3-1\right)^2\cos(4q)+4\left(a_0^6-1\right)\cos(2q)-5a_0^6+2a_0^3-5\right)=0, \tag{23}$$

$$2a_0^2(\alpha\xi+1)q''+2\alpha a_0^2q'+2\eta^2\left(a_0^3-1\right)(\alpha\xi+1)V'\left(\cos^2q-a_0^3\sin^2q\right)+\alpha\eta^2V\left(\left(a_0^3-1\right)^2-\left(a_0^6-1\right)\cos(2q)\right)=0. \tag{24}$$

These two equations must be solved together with the boundary conditions

$$V(0)=V(1)=0, \quad q(0)=q(1)=0. \tag{25}$$

The parameter α governs the aspect ratio of the channel, and the flat-channel limit, as studied in Ref. [15], is recovered when $\alpha = 0$.

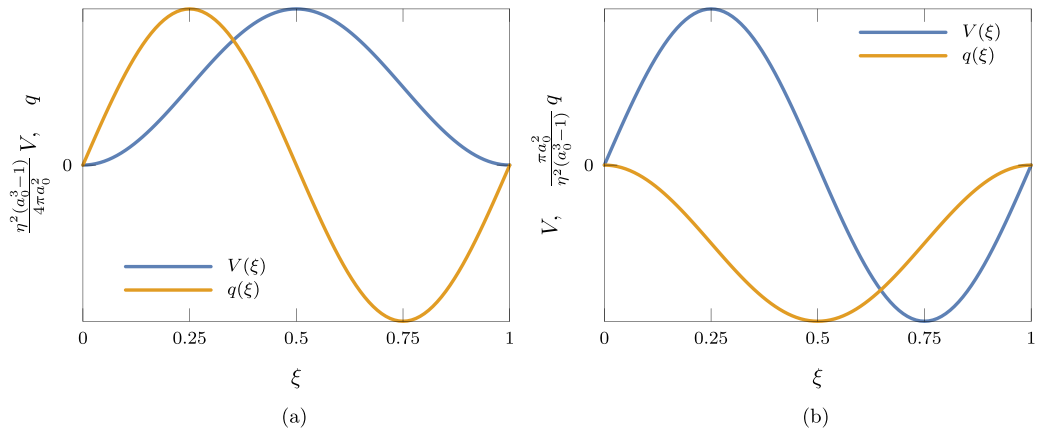

FIG. 2. Schematic profiles illustrating bifurcation modes in a straight channel case, as given by Eq. (33). The blue lines represent the velocity profiles, while the orange lines pertain to the director field. The figures correspond to: (a) One-directional flow, $C_1 = 1$ and $C_2 = 0$; (b) Bi-directional flow, $C_1 = 0$ and $C_2 = 1$.

Setting $\alpha = 0$ in Eqs. (23) and (24), we obtain

$$q'\left[8\left(a_0^3-1\right)\left(a_0^3\cos^2 q+\sin^2 q\right)\sin(2q)V' - 4a_0\left(a_0^3-1\right)\zeta\cos(2q)\right] + V''\left[a_0^3(\cos(4q)-1) + 2a_0^6(\cos(2q)+3)\sin^2 q - 2(\cos(2q)-3)\right]\cos^2 q = 0, \tag{26a}$$

$$2a_0^2 q'' + \eta^2 V'\left[\left(a_0^6-1\right)\cos(2q) - \left(a_0^3-1\right)^2\right] = 0, \tag{26b}$$

which are equivalent to the Eqs. (27a) and (27b) in Ref. [15].

IV. BIFURCATION ANALYSIS

The problem under consideration possesses a principal branch of solutions, namely a trivial solution with $V = 0$ and $q = 0$, for all values of the parameters α, η, and ζ. We aim to investigate the existence of nontrivial solutions that represent small perturbations of $V = 0$ and $q = 0$. To this end, we consider the linear approximation of Eqs. (23) and (24) for small V and q. It is feasible to utilize Eq. (24) to eliminate q'' from Eq. (23), yielding, after algebraic manipulation, the following:

$$V'' + \frac{\alpha V'}{1+\alpha\xi} - \frac{\alpha^2 V}{(1+\alpha\xi)^2} - \zeta a_0\left(a_0^3-1\right)q' - \frac{2\alpha\zeta a_0\left(a_0^3-1\right)}{(1+\alpha\xi)}q = 0, \tag{27}$$

$$q'' + \frac{\alpha q'}{1+\alpha\xi} + \eta^2\frac{a^3-1}{a_0^2}V' - \frac{\alpha\eta^2}{1+\alpha\xi}\frac{a_0^3-1}{a_0^2}V = 0. \tag{28}$$

We initially examine the near-planar case, specifically when $\alpha = h/r_1 \ll 1$ and employ the following asymptotic expansion:

$$V(\xi) = V_0(\xi) + \alpha V_1(\xi) + o(\alpha), \tag{29a}$$

$$q(\xi) = q_0(\xi) + \alpha q_1(\xi) + o(\alpha). \tag{29b}$$

A. Straight-channel case

The leading-order equations are obtained by setting $\alpha = 0$ in Eqs. (27) and (28). We find

$$V_0'' - \zeta\, a_0\left(a_0^3-1\right)q_0' = 0, \tag{30a}$$

$$q_0'' + \eta^2\frac{a_0^3-1}{a_0^2}V_0' = 0. \tag{30b}$$

These correspond to the equations for a perfectly flat domain, that is, the case in which the nematic is confined between two parallel planes separated by a distance h. When solving Eqs. (30a) and (30b), subject to the boundary conditions $V_0(0) = V_0(1) = 0$ and $q_0(0) = q_0(1) = 0$, only the trivial solution is obtained unless the activity ζ assumes one of the critical values:

$$\zeta = \frac{4\pi^2 a_0}{\left(a_0^3-1\right)^2\eta^2}n^2, \quad n \in \mathbb{Z}\setminus\{0\}. \tag{31}$$

We choose the smallest value and set

$$\zeta_0 = \frac{4\pi^2 a_0}{\left(a_0^3-1\right)^2\eta^2}, \tag{32}$$

in which case the bifurcating branches have the solutions

$$V_0(\xi) = C_1 \frac{4\pi a_0^2}{\eta^2\left(a_0^3-1\right)} \sin^2(\pi\,\xi) + C_2 \sin(2\pi\,\xi), \quad (33a)$$

$$q_0(\xi) = C_1 \sin(2\pi\,\xi) - C_2 \frac{\eta^2\left(a_0^3-1\right)}{\pi a_0^2} \sin^2(\pi\,\xi), \quad (33b)$$

where C_1 and C_2 are two arbitrary integration constants. A detailed analysis of the system through weakly nonlinear methods, as outlined in [15], reveals precisely two distinct flow behaviors:

(a) One-directional flow: Occurs when $C_1 \neq 0$ and $C_2 = 0$. This configuration results in a net flow moving consistently in one direction.

(b) Bi-directional flow: Emerges when $C_1 = 0$ and $C_2 \neq 0$. This condition leads to the development of two opposing flow bands, each moving in opposite directions.

These findings reveal that, under identical critical conditions, the system can exhibit two fundamentally different flow and alignment director patterns (see Fig. 2). The authors in Ref. [21] show that this degeneracy is due to the geometric and physical symmetry inherent in the planar problem.

B. Small aspect-ratio limit

To account for the first-order corrections due to the channel curvature, let us consider the next order of approximation in the expansion of the Eqs. (27) and (28) with respect to the channel aspect ratio α. To find the first order correction to the critical activity we posit

$$\zeta = \zeta_0(1 + \alpha\,\nu) + o(\alpha), \quad (34)$$

where ν is yet to be determined, and retain the $O(\alpha)$ terms in the expansion of Eqs. (23) and (24). After the substitution of $V_0(\xi)$ and $q_0(\xi)$, as given in Eqs. (33a) and (33b), we are led to consider the following system of linear differential equations

$$V_1'' - \frac{4\pi^2 a_0^2}{\eta^2\left(a_0^3-1\right)} q_1' = \frac{4\pi^2 C_1(2\pi\,\nu\cos(2\pi\xi) + \sin(2\pi\xi))a_0^2}{\eta^2\left(a_0^3-1\right)} - 2\pi C_2(2 - \cos(2\pi\xi) + 2\pi\,\nu\sin(2\pi\xi)), \quad (35a)$$

$$q_1'' + \eta^2 \frac{a_0^3-1}{a_0^2} V_1' = 2\pi C_1(2\cos(2\pi\xi) - 1) + \frac{2\eta^2 C_2 \sin(2\pi\xi)\left(a_0^3-1\right)}{a_0^2}, \quad (35b)$$

which is to be solved with respect to the unknown functions $V_1(\xi)$, $q_1(\xi)$, and the parameter ν, together with the boundary conditions

$$V_1(0) = V_1(1) = 0, \quad q_1(0) = q_1(1) = 0. \quad (36)$$

The mathematical structure of Eq. (35) can be expressed as $L\boldsymbol{x} = \mathbf{b}$, where $\boldsymbol{x} = (V_1, q_1)$ is the vector of unknown functions, $L : (H^1(0,1))^2 \to (L^2(0,1))^2$ is a linear operator defined by the left-hand side of Eqs. (35a) and (35b) [which is identical to that of Eqs. (30)], and $\mathbf{b}$ is the vector defined by the right-hand side of Eqs. (35a) and (35b). According to the Fredholm alternative, the system is solvable for $\boldsymbol{x}$ if and only if the right-hand side, $\mathbf{b}$, is orthogonal to the null space, $\ker(L^\dagger)$, of the adjoint operator $L^\dagger$. By a repeated use of integration by parts, the formal adjoint of L, with respect to the $L^2(0,1)^2$ inner product, is found to be

$$L^\dagger \begin{pmatrix} \phi_1 \\ \phi_2 \end{pmatrix} = \begin{pmatrix} \phi_1'' - \Omega\phi_2' \\ \phi_2'' + \frac{4\pi^2}{\Omega}\phi_1' \end{pmatrix}, \quad (37)$$

with $\Omega = \eta^2 \frac{a_0^3-1}{a_0^2}$, and boundary conditions $\phi_1(0) = \phi_1(1) = 0$, $\phi_2(0) = \phi_2(1) = 0$. Hence, $\ker(L^\dagger)$ is generated by the two vectors

$$\mathbf{u}_1 = (u_{11}, u_{12}) = \left(\sin(2\pi\xi),\ -\frac{4\pi a_0^2}{\eta^2\left(a_0^3-1\right)}\sin^2(\pi\xi)\right),$$

$$\mathbf{u}_2 = (u_{21}, u_{22}) = \left(\frac{\eta^2\left(a_0^3-1\right)}{\pi a_0^2}\sin^2(\pi\xi),\ \sin(2\pi\xi)\right),$$

and we get two solvability conditions, $\langle \mathbf{b}, \mathbf{u}_1 \rangle_{L^2} = 0$ and $\langle \mathbf{b}, \mathbf{u}_2 \rangle_{L^2} = 0$, more explicitly written as

$$\int_0^1 (b_1 u_{11} + b_2 u_{12}) d\xi = 0, \quad (38a)$$

$$\int_0^1 (b_1 u_{21} + b_2 u_{22}) d\xi = 0. \quad (38b)$$

After some algebra, these conditions rewrite as

$$\frac{3a_0^2}{\eta^2\left(a_0^3-1\right)} C_1 + \nu\, C_2 = 0, \quad (39a)$$

$$\nu\, C_1 + \frac{3\eta^2\left(a_0^3-1\right)}{4\pi^2 a_0^2} C_2 = 0. \quad (39b)$$

At the critical point, the leading-order amplitudes, C_1 and C_2, cannot both be equal to zero. This implies that the coefficient matrix of Eqs. (39a) and (39b) must have a zero determinant. This condition yields and equation for ν, given by

$$\nu^2 = \frac{9}{4\pi^2}, \quad (40)$$

which also introduces two distinct corrections to the critical threshold ζ_0, thereby breaking the degeneracy observed in the planar case. Furthermore, the linear system described in Eq. (39) establishes relationships between the leading-order amplitudes of the solution (33). Therefore, we identify two possible solutions:

$$\nu_- = -\frac{3}{2\pi}, \quad C_2 = \frac{2\pi a_0^2}{\eta^2\left(a_0^3-1\right)} C_1, \quad (41)$$

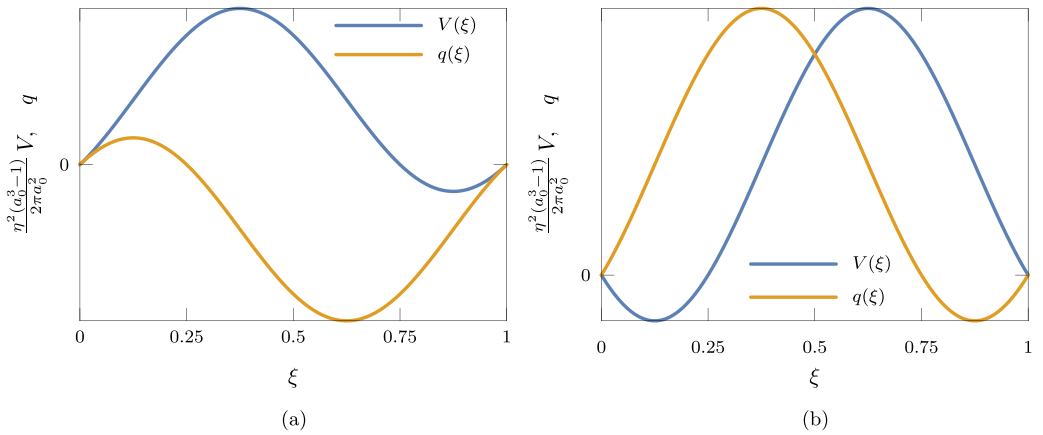

FIG. 3. Schematic profiles of linear bifurcation modes in the small aspect-ratio limit. The blue lines depict the velocity profiles, and the orange lines represent the director field. The figures illustrate: (a) the lower critical threshold solution as specified in Eq. (44), featuring a counter-propagating layer near the outer boundary; (b) the higher critical threshold solution as specified in Eq. (46), with a counter-propagating layer near the inner boundary.

and

$$\nu_+ = \frac{3}{2\pi}, \quad C_2 = -\frac{2\pi a_0^2}{\eta^2\left(a_0^3-1\right)} C_1. \tag{42}$$

In contrast to the planar problem discussed in [15], the first-order correction introduces a distinction in the critical threshold, resulting in two distinct critical values:

(a) The lower critical threshold (which is the actual critical value):

$$\zeta_{\mathrm{cr}_-} = \zeta_0(1+\alpha\nu_-) = \frac{2\pi(2\pi r_1 - 3h)\kappa a_0}{h^2\mu r_1\left(a_0^3-1\right)^2}. \tag{43}$$

Corresponding to this threshold, the leading order solution is given by:

$$V_0(\xi) = C_1 \frac{2\pi a_0^2}{\eta^2\left(a_0^3-1\right)}(2\sin^2(\pi\xi) + \sin(2\pi\xi)), \tag{44a}$$

$$q_0(\xi) = C_1(\sin(2\pi\xi) - 2\sin^2(\pi\xi)). \tag{44b}$$

(b) The higher critical threshold:

$$\zeta_{\mathrm{cr}_+} = \zeta_0(1+\alpha\nu_+) = \frac{2\pi(2\pi r_1 + 3h)\kappa a_0}{h^2\mu r_1\left(a_0^3-1\right)^2}. \tag{45}$$

Corresponding to this threshold, the leading order solution is given by:

$$V_0(\xi) = C_1 \frac{2\pi a_0^2}{\eta^2\left(a_0^3-1\right)}(2\sin^2(\pi\xi) - \sin(2\pi\xi)), \tag{46a}$$

$$q_0(\xi) = C_1(\sin(2\pi\xi) + 2\sin^2(\pi\xi)). \tag{46b}$$

The velocity and director profiles are shown in Fig. 3. We can, therefore, conclude that the curved wall breaks the double degeneracy of the solution at the bifurcation threshold set for the plane case discussed in [15]. The critical threshold, up to $O(\alpha)$, is given by Eq. (43), and the solution profile, up to a constant, is given by Eqs. (44a) and (44b). The red lines in Fig. 4 show how the critical thresholds, given by Eq. (43) and Eq. (45), branch off from the straight-channel case.

C. Large aspect-ratio limit

When α is large, the regular expansion in terms of α employed in the previous paragraph becomes inapplicable. To investigate the trend of the critical threshold as the channel curvature varies, we introduce a change of variables to simplify Eqs. (27) and (28).

Equation (27) is used to derive V'', while Eq. (28) is employed to determine V'. Subsequently, we differentiate Eq. (28) and substitute the expressions obtained previously for

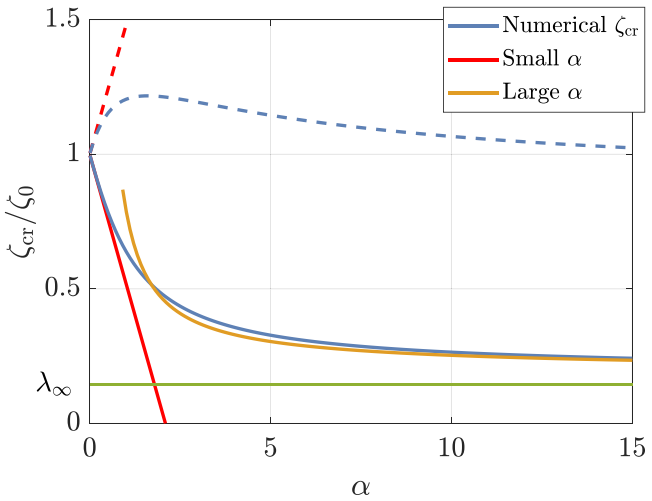

FIG. 4. This figure illustrates the variation of the critical threshold (normalized to the planar case threshold) with the aspect ratio, α. The dashed lines show the higher critical threshold. The two blue lines represent the thresholds for the first and second bifurcation modes. These thresholds coincide at $\alpha = 0$; the curvature of the domain thus separates them. The red lines, given by Eqs. (43) (solid) and (45) (dashed), respectively, show the approximations of these thresholds for small α (very narrow channel). The yellow line represents the lower threshold in the large α limit (thick domain), as given by Eq. (58). The horizontal green line indicates the lower bound of the critical activity as α tends to infinity.

V'' and V'. In doing so, we eliminate the variable V, resulting in a third-order equation solely in terms of q:

$$q''' + \frac{\alpha q''}{\alpha\xi + 1} + \left(\frac{\left(a_0^3 - 1\right)^2 \zeta \eta^2}{a_0} - \frac{\alpha^2}{(\alpha\xi + 1)^2}\right) q' + \frac{2\alpha\zeta\eta^2\left(a_0^3 - 1\right)^2}{a_0(\alpha\xi + 1)} q = 0, \tag{47}$$

while the velocity field V can be determined using one of the previous equations.

By defining the rescaled variable x and the functions $y(x)$ and $z(x)$ as follows:

$$\lambda := \zeta/\zeta_0, \quad x := 2\pi\sqrt{\lambda}\left(\xi + \frac{1}{\alpha}\right), \tag{48}$$

$$y(x) := q(\xi)|_{\xi = \frac{x}{2\pi\sqrt{\lambda}} - \frac{1}{\alpha}}, \tag{49}$$

$$z(x) := \left.\frac{\eta^2\left(a_0^3 - 1\right)}{2\pi\lambda a_0^2} V(\xi)\right|_{\xi = \frac{x}{2\pi\sqrt{\lambda}} - \frac{1}{\alpha}}, \tag{50}$$

where ζ_0 is the critical threshold in the planar case, as defined in Eq. (32), all geometric and material parameters can be absorbed into the definition of the unknown functions. Consequently, the linearized Eqs. (47) and (28) can be rewritten as:

$$y''' + \frac{3y''}{x} + \left(1 + \frac{1}{x^2}\right) y' + \frac{2y}{x} = 0, \tag{51}$$

$$z' - \frac{z}{x} + y' + \frac{y'}{x} = 0. \tag{52}$$

The (homogeneous) boundary conditions at $\xi = 0$ and $\xi = 1$ become, respectively,

$$y(2\pi\sqrt{\lambda}/\alpha) = z(2\pi\sqrt{\lambda}/\alpha) = 0, \tag{53}$$

$$y(2\pi\sqrt{\lambda}(1 + 1/\alpha)) = z(2\pi\sqrt{\lambda}(1 + 1/\alpha)) = 0. \tag{54}$$

Although the general solution of Eqs. (51) and (52) can be expressed in terms of special functions, this representation can become cumbersome. A more convenient approach is to approximate the solutions using a Frobenius series expansion about the singular point $x = 0$ (see [31]). Since the integration interval is defined by the domain limits $x_1 = 2\pi\sqrt{\lambda}/\alpha$ and $x_2 = 2\pi\sqrt{\lambda}(1 + 1/\alpha)$, and as the two equations do not exhibit finite singularities other than zero, the Frobenius series possesses an infinite radius of convergence. Consequently, we expect the truncated series to yield an accurate approximation of the solution, particularly in the limit of $\alpha \gg 1$.

Truncating the expansion to $O(x^6)$, we find

$$y(x) = k_1\left(1 - \frac{x^2(x^4 - 36x^2 + 576)}{2304}\right) + k_2\left(\frac{(11x^4 - 324x^2 + 3456)x^2}{13824} + \left(1 - \frac{x^2(x^4 - 36x^2 + 576)}{2304}\right)\log x\right) + k_3\left[-\frac{97x^6}{55296} + \frac{23x^4}{512} - \frac{3x^2}{8} + \left(\frac{11x^6}{6912} - \frac{3x^4}{64} + \frac{x^2}{2}\right)\log x + \left(1 - \frac{x^2(x^4 - 36x^2 + 576)}{2304}\right)(\log x)^2\right] + o(x^6), \tag{55}$$

$$z(x) = k_1\left(\frac{1}{256}(x^2 - 32)x^3 + x\log x\right) + k_2\left(-\frac{7x^5}{1024} + \frac{3x^3}{16} + \frac{1}{256}(x^2 - 32)x^3\log x + \frac{1}{2}x(\log x)^2\right) + k_3\left[\frac{15x^5}{1024} - \frac{3x^3}{8} + \left(\frac{3x^3}{8} - \frac{7x^5}{512}\right)\log x + \frac{1}{256}(x^2 - 32)x^3(\log x)^2 + \frac{1}{x} + \frac{1}{3}x(\log x)^3\right] + k_4 x + o(x^6). \tag{56}$$

Imposing the homogeneous boundary conditions (54), yields a homogeneous linear system for the unknown parameters k_1, k_2, k_3, and k_4. The bifurcation condition arises from the requirement that this system possess nontrivial solutions, i.e., the determinant of the coefficient matrix must vanish. For brevity, the explicit calculations, while straightforwardly obtainable using symbolic manipulation software, such as Mathematica, are omitted here.

The leading order of the bifurcation equation is given by

$$\pi^2\lambda(11\pi^4\lambda^2 - 81\pi^2\lambda + 216) - 6(\pi^6\lambda^3 - 9\pi^4\lambda^2 + 36\pi^2\lambda - 36)\log(1 + \alpha) = 0, \tag{57}$$

which implicitly defines the relationship between the critical threshold $\lambda_{cr}(\alpha) = \zeta_{cr}(\alpha)/\zeta_0$ and the aspect ratio parameter α.

An explicit expression for the critical threshold can be obtained by performing an asymptotic expansion of Eq. (57) in terms of the gauge function $(\log(1 + \alpha))^{-k}$, with $k \in \mathbb{N}$. For $\alpha \to +\infty$, this yields

$$\frac{\zeta_{cr}(\alpha)}{\zeta_0} \sim \lambda_\infty + \frac{\lambda_1}{\log(1 + \alpha)} + \frac{\lambda_2}{(\log(1 + \alpha))^2}, \tag{58}$$

where numerical evaluation yields $\lambda_\infty \approx 0.144889$, $\lambda_1 \approx 0.180674$, and $\lambda_2 \approx 0.187739$. Here, λ_∞ represents the finite limiting value of the critical threshold, as the curvature parameter α tends to infinity. Hence, curvature is shown to promote spontaneous flow, lowering the critical threshold.

V. DISCUSSION

We performed numerical simulations of the fully nonlinear problem using MATLAB's bvp4c function to validate our previous analytical results and analyze solution behavior far from the critical threshold at high activity levels. Specifically, we numerically solved the nonlinear problem defined by Eqs. (23)

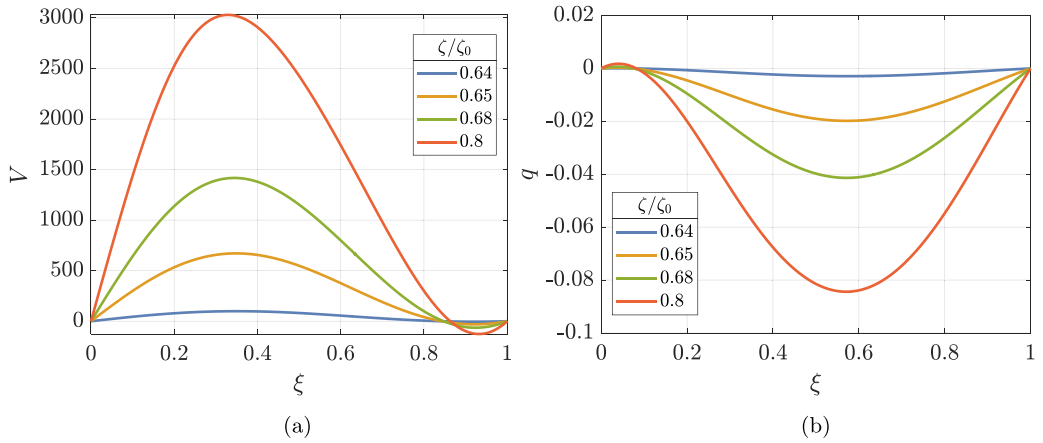

FIG. 5. Numerically obtained velocity (a) and director (b) profiles for the principal mode (lower threshold) from the nonlinear problem. Profiles are shown for different values of the activity coefficient, with fixed parameters $\alpha = 1$, $a_0 = 1.8$, and $\eta = 0.01$.

and (24) with the boundary conditions in Eq. (25). The bifurcation threshold was determined using Eqs. (27) and (28).

Figure 5 illustrates typical velocity and director profiles of the principal mode (the one with the lower threshold), which were derived from numerical solutions to the nonlinear problem using $\alpha = 1$, $a_0 = 1.8$, and $\eta = 0.01$. The profiles are shown for various values of the activity coefficient and are intended for comparison with the linear solutions in Fig. 3.

Numerical solutions allow us to study the behavior of the critical threshold in the intermediate regime of α (see Fig. 4) and confirm the analytical results of Sec. IV in the cases of small and large α.

Furthermore, we observe that, in line with the analytical predictions, the presence of a curved profile breaks the symmetry of the planar case. In other words, the planar configuration represents a degenerate case in which the critical thresholds of the first two modes coincide. As a result, in the planar case, two distinct solution branches emerge at the same critical threshold: one characterized by the onset of motion in a single direction, and the other exhibiting two counter-propagating bands. The curvature of the domain induces a separation between the thresholds, and this effect increases with α, thus promoting the spontaneous flow represented by the mode corresponding to the smallest critical threshold. However, as shown in Eq. (58), there is a lower bound λ_∞ for the critical threshold, in the limit of vanishing internal radius. The numerical curve slowly tends towards this limit, with logarithmic convergence, as α increases.

To highlight the differences between the modes of the curved channel and those of the planar case, we project the numerical solution onto the planes spanned by the linear solutions in the planar case. More precisely, the Fourier components of the planar-channel modes contained in the numerical solutions are calculated by taking the L^2-inner product of the numerical solution with the two linear planar solutions, as given in Eqs. (33a) and (33b), suitably normalized. The results for $\alpha = 0$ and $\alpha = 0.2$ are shown in Fig. 6, while the corresponding orthogonal projections onto the horizontal, vertical, and A_1A_2 planes are presented in Fig. 7.

The fact that the vertices of the two branches do not coincide stems from the threshold separation in the nonplanar case, see Figs. 7(d) and 7(e). Furthermore, the observation that the curves do not lie within the planes $A_1 = 0$ and $A_2 = 0$ shows that, in the nonplanar solution, mode mixing occurs already at the bifurcation point, as explicitly inferred from Eqs. (44) and (46).

The numerical solution clearly highlights the presence of a counter-propagating layer near the outer boundary of the circular domain, as predicted by the solutions of Eq. (44) for the linearized problem and confirmed by the velocity profile shown in Fig. 3(a). The thickness ξ_0 of this layer is influenced both by the activity and by the value of α. This result is qualitatively in agreement with the experimental findings of [4,5,29], where the formation of a counter-propagating layer near the outer boundary of the domain is observed in some circumstances. A more realistic representation of the experiments should incorporate an analysis with varied boundary conditions, such as applying Neumann conditions at the inner boundary for both the velocity and director fields. In addition, more complex models could be considered including, for example, concentration as an additional field. This could be an objective for future research.

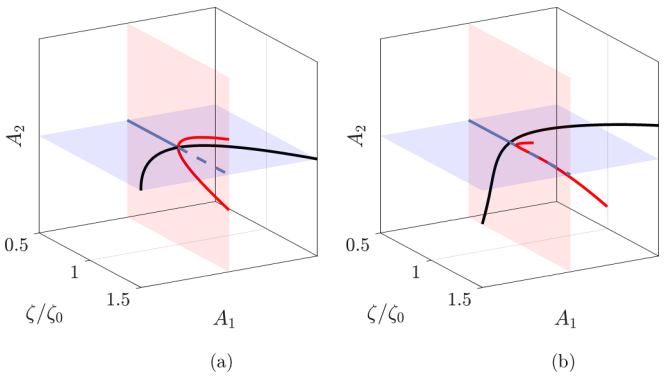

FIG. 6. Bifurcation diagrams for $\eta = 0.01$, and $a_0 = 1.8$, comparing the cases (a) $\alpha = 0$ and (b) $\alpha = 0.2$. In (a) the bifurcation follows a standard pitchfork structure, while in (b) the introduction of $\alpha = 0.2$ deforms the diagram, leading to two nonplanar pitchfork with different vertices. This deformation indicates a coupling between the two modes, resulting in a different solution landscape.

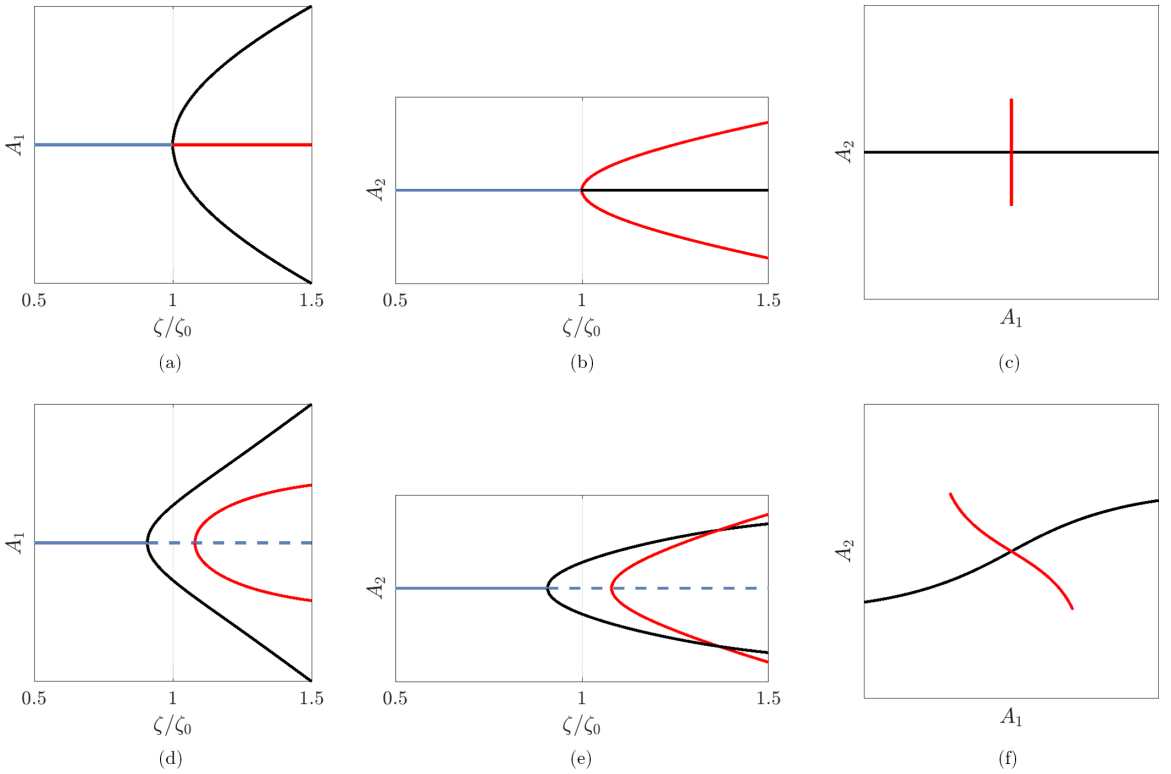

FIG. 7. Amplitude diagrams for $\eta = 0.01$, and $a_0 = 1.8$, projected onto the vertical, horizontal, and A_1A_2 planes for (a)–(c) $\alpha = 0$ and (d)–(f) $\alpha = 0.2$. These projections reveal the separation and relative shift of the two pitchfork branches, illustrating the breaking of degeneracy in the critical activity. As a result, two bifurcations result at distinct lower and higher critical values. Plots (c) and (f) also reveal that the planar modes mixes at the bifurcation value, so that red and black lines do not have vertical and horizontal tangent in the origin.

To gain a deeper understanding of this phenomenon, we investigated how its thickness depends on the activity and the aspect ratio of the annular region; the results are presented in Fig. 8. High values of activity or α tend to suppress the layer, to the point where it may no longer be practically observable. However, for a given value of α, the layer reaches its maximum extent at the critical threshold. Nevertheless, the counter-propagating layer never exceeds 25% of the thickness of the annular region, as can be deduced from Fig. 8, Fig. 3(a), and Eq. (44a).

Interestingly, Figure 3(b) suggests a possible opposite scenario, where the counter-propagating layer forms near the

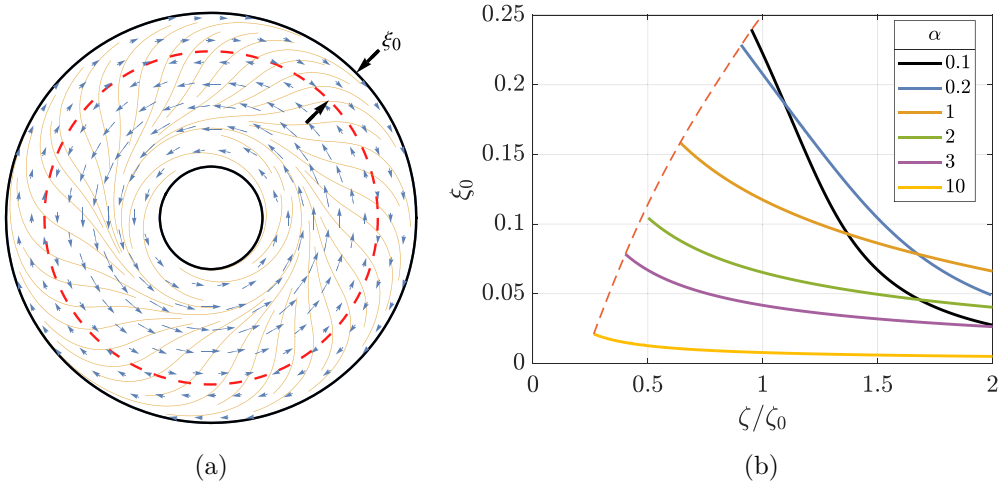

FIG. 8. (a) Schematic representation of the velocity and director profiles. The blue arrows indicate the velocity field, while the orange lines depict the director field. The red dashed line marks the separation between the counter-propagating regions. The dimensionless parameter ξ_0 measures the ratio between the depth of the counter-propagating layer near the outer boundary and the annulus thickness h. (b) Counter-propagating layer thickness ξ_0 as a function of activity for different values of the aspect-ratio α, with $\eta = 0.01$ and $a_0 = 1.8$. The red dashed line marks the boundary of the critical region, beyond which no spontaneous flow occurs.

inner boundary of the domain. However, this effect involves the second bifurcation mode and, therefore, would occur only at a higher critical activity threshold.

Counter-propagating boundary-layers have also been observed in other experimental and numerical studies. For example, Hardoüin *et al.* [24] study spontaneous flow in filamentous bundles of microtubules and kinesin molecular motors at the water/oil interface. They observe distinct flow patterns near the boundary, which they term 'active boundary layers' (ABLs). These ABLs are characterized by the accumulation of negative topological defects at the wall, a phenomenon they attribute to bend instabilities leading to defect pair unbinding, where $+1/2$ defects are ejected into the bulk while negative defects remain at the boundary.

The importance of confinement is also apparent in other numerical and analytical works [26,27]. Joshi *et al.* [26] explore active nematic dynamics in annular geometries using simulations and reveal curvature-driven states which embodies corotating defects. Luo *et al.* [27] examines active Couette flows in channels with external shear, finding that shear can stabilize extensile or destabilize contractile fluids, leading to unidirectional, oscillatory, or dancing flows. Curvature in annular channels further modifies these flow states compared to straight channels.

However, the phenomena described [24,26,27] are fundamentally different from ours, since we analyze a laminar motion, in the absence of defects or externally imposed shear, but in agreement with Wioland's work on bacterial motion [4,5], where a turbulent regime is not typically observed.

Therefore, these phenomena appear to be essentially distinct. This divergence could be attributed to several factors, including the level of activity studied (as turbulence generally emerges at higher activity levels) or the specific type of active nematic system analyzed. For instance, the microtubule-based system used by Hardoüin *et al.* might have different propensities for turbulence and defect formation compared to other systems, such as bacteria colonies.

VI. CONCLUSIONS

In this work, we have analyzed the spontaneous flow of active nematics confined within an annular domain, employing a continuum mechanics approach for materials with relaxation. Our investigation focused on the influence of the channel's aspect ratio on the onset of spontaneous motion and the emerging velocity profile. Through a combination of bifurcation analysis and numerical simulations, we have provided a comprehensive characterization of the role of curvature in breaking the degeneracy observed in the planar case.

Specifically, we demonstrated that the presence of curvature lowers the activity threshold required for the onset of spontaneous flow. This effect becomes more pronounced as the aspect ratio α increases, facilitating spontaneous motion compared to the flat channel case.

In a planar channel, two distinct flow configurations—a unidirectional flow and a counter-propagating banded structure—emerge at the same critical threshold, leading to a degeneracy in the bifurcation structure. In contrast, the curved geometry introduces a separation in the critical thresholds of these two modes, favoring the emergence of a solution with a thinner counter-propagating band near the outer boundary.

By performing a systematic asymptotic expansion for both small and large aspect-ratio limits, we derived explicit corrections to the critical activity threshold. For large α, we showed that the threshold asymptotically approaches a lower bound, scaling as $\zeta_{cr}/\zeta_0 \approx 0.144889 + O(1/\log(1+\alpha))$, indicating that curvature has a fundamental role in promoting spontaneous flow. These analytical predictions are also confirmed by numerical simulations.

Furthermore, the numerical results clearly show the presence of a counter-propagating layer near the outer boundary of the domain. The thickness of this layer is influenced by both activity and aspect ratio.

Our findings provide insight into the interplay between confinement, curvature, and spontaneous flow in active nematics. They are particularly relevant in the context of biological systems, where curvature-induced flow phenomena are frequently observed, such as in confined bacterial colonies. Future research directions include extending this framework to incorporate order parameter variations, topological defects, and turbulent active flows in more complex geometries.

ACKNOWLEDGMENTS

The work has been funded by the MUR Project PRIN 2020, Italy, Mathematics for Industry 4.0 (Project No. 2020F3NCPX). S.T. also acknowledges the partial support by MUR, Italy, Grant Dipartimento di Eccellenza 2023–2027. This research was also conducted under the auspices of the GNFM-INdAM.

DATA AVAILABILITY

The data are not publicly available. The data are available from the authors upon reasonable request.

APPENDIX: STRESS TENSOR

In this Appendix, we detail the calculations leading to the expression for the stress tensor as a function of the velocity field, $\mathbf{v}$, and the angle, θ. By selecting $\mathbf{v}$ to represent a shear motion along the azimuthal direction, specifically $\mathbf{v} = v(r)\mathbf{e}_\varphi$, we can readily derive the following results:

$$\nabla\mathbf{v} = v'(\mathbf{e}_\varphi \otimes \mathbf{e}_r) - \frac{v}{r}(\mathbf{e}_\varphi \otimes \mathbf{e}_\varphi). \tag{A1}$$

The director field is parametrized as

$$\mathbf{n} = \sin\theta(r)\mathbf{e}_r + \cos\theta(r)\mathbf{e}_\varphi, \tag{A2}$$

so that its spatial gradient may then be expressed as

$$\nabla\mathbf{n} = \theta'\cos\theta\ (\mathbf{e}_r \otimes \mathbf{e}_r) + \frac{\sin\theta}{r}\ (\mathbf{e}_\varphi \otimes \mathbf{e}_\varphi) - \frac{\cos\theta}{r}\ (\mathbf{e}_r \otimes \mathbf{e}_\varphi) - \theta'\sin\theta\ (\mathbf{e}_\varphi \otimes \mathbf{e}_r). \tag{A3}$$

By substituting Eq. (13) into Eq. (1), we obtain an expression for the shape tensor:

$$\mathbf{L} = \frac{1}{a_0}\begin{pmatrix} \left(a_0^3-1\right)\sin^2\theta + 1 & \cos\theta\sin\theta\left(a_0^3-1\right) \\ \cos\theta\sin\theta\left(a_0^3-1\right) & \left(a_0^3-1\right)\cos^2\theta + 1 \end{pmatrix}. \quad \text{(A4)}$$

To determine the stress tensor, we need the codeformational derivative of $\mathbf{L}$, defined as

$$\mathbf{L}^{\triangledown} := \frac{\partial \mathbf{L}}{\partial t} + (\nabla \mathbf{L})\mathbf{v} - (\nabla \mathbf{v})\mathbf{L} - \mathbf{L}(\nabla \mathbf{v})^{\top}. \quad \text{(A5)}$$

In a steady state, i.e., $\frac{\partial \mathbf{L}}{\partial t} = 0$, this simplifies to

$$\mathbf{L}^{\triangledown} = \frac{v - rv'}{ra_0}\begin{pmatrix} 0 & \left(a_0^3-1\right)\sin^2\theta + 1 \\ \left(a_0^3-1\right)\sin^2\theta + 1 & \left(a_0^3-1\right)\sin(2\theta) \end{pmatrix}. \quad \text{(A6)}$$

Finally, substituting Eq. (A6) into Eq. (10) yields the Cauchy stress tensor, with the following components:

$$T_{rr} = -p - \rho\kappa\theta'^2 - \frac{\rho\mu}{2a_0^2 r}\left[\left(a_0^3-1\right)\sin^2\theta + 1\right]\left[2a_0\zeta r + \left(a_0^3-1\right)\tau\sin(2\theta)(v - rv')\right], \quad \text{(A7)}$$

$$T_{r\varphi} = \rho\kappa\frac{\theta'}{r} - \frac{\rho\mu}{2a_0^2 r}\left[a_0\left(a_0^3-1\right)\zeta r\sin(2\theta) + 2\tau\left(\left(a_0^3-1\right)\sin^2\theta + 1\right)\left(\left(a_0^3-1\right)\cos^2\theta + 1\right)(v - rv')\right], \quad \text{(A8)}$$

$$T_{\varphi r} = \rho\kappa\frac{\theta'}{r} - \frac{\rho\mu}{2a_0^2 r}\left[a_0\left(a_0^3-1\right)\zeta r\sin(2\theta) + 2\tau\left(\left(\left(a_0^3-1\right)\sin^2\theta + 1\right)^2 + \frac{1}{2}\left(a_0^3-1\right)^2\sin^2(2\theta)\right)(v - rv')\right], \quad \text{(A9)}$$

$$T_{\varphi\varphi} = -p - \frac{\rho\kappa}{r^2} - \frac{\rho\mu}{2a_0^2 r}\left[2a_0\zeta r\left(\left(a_0^3-1\right)\cos^2\theta + 1\right) + \frac{\tau}{2}\left(a_0^3-1\right)\sin(2\theta)\left(\left(a_0^3-1\right)\cos(2\theta) + 3\left(a_0^3+1\right)\right)(v - rv')\right]. \quad \text{(A10)}$$

[1] T. Sanchez, D. T. Chen, S. J. DeCamp, M. Heymann, and Z. Dogic, Nature (London) **491**, 431 (2012).
[2] M. Piel and R. Voituriez, in *The Oxford Handbook of Soft Condensed Matter* (Oxford University Press, Oxford, 2015), Chap. 12.
[3] D. Volfson, S. Cookson, J. Hasty, and L. S. Tsimring, Proc. Natl. Acad. Sci. USA **105**, 15346 (2008).
[4] H. Wioland, F. G. Woodhouse, J. Dunkel, J. O. Kessler, and R. E. Goldstein, Phys. Rev. Lett. **110**, 268102 (2013).
[5] H. Wioland, E. Lushi, and R. E. Goldstein, New J. Phys. **18**, 075002 (2016).
[6] A. Cavagna and I. Giardina, Annu. Rev. Condens. Matter Phys. **5**, 183 (2014).
[7] I. W. Stewart, *The Static and Dynamic Continuum Theory of Liquid Crystals: A Mathematical Introduction* (Taylor & Francis, New York, 2004).
[8] R. A. Simha and S. Ramaswamy, Phys. Rev. Lett. **89**, 058101 (2002).
[9] R. Voituriez, J.-F. Joanny, and J. Prost, Europhys. Lett. **70**, 404 (2005).
[10] S. A. Edwards and J. M. Yeomans, Europhys. Lett. **85**, 18008 (2009).
[11] G. Gonnella, D. Marenduzzo, A. Suma, and A. Tiribocchi, C. R. Phys. **16**, 316 (2015).
[12] S. Bhattacharyya and J. M. Yeomans, Phys. Rev. Lett. **130**, 238201 (2023).
[13] E. Tjhung, D. Marenduzzo, and M. E. Cates, Proc. Natl. Acad. Sci. USA **109**, 12381 (2012).
[14] L. Giomi and A. DeSimone, Phys. Rev. Lett. **112**, 147802 (2014).
[15] S. S. Turzi, Phys. Rev. E **96**, 052603 (2017).
[16] S. Turzi, Proc. R. Soc. A **479**, 20220564 (2023).
[17] L. Giomi, L. Mahadevan, B. Chakraborty, and M. F. Hagan, Nonlinearity **25**, 2245 (2012).
[18] D. Marenduzzo, E. Orlandini, M. E. Cates, and J. M. Yeomans, Phys. Rev. E **76**, 031921 (2007).
[19] D. Marenduzzo, E. Orlandini, and J. M. Yeomans, Phys. Rev. Lett. **98**, 118102 (2007).
[20] J. Walton, G. McKay, M. Grinfeld, and N. J. Mottram, Eur. Phys. J. E **43**, 51 (2020).
[21] A. Marzorati and S. Turzi, J. Phys. A: Math. Theor. **56**, 315601 (2023).
[22] S. Chen, P. Gao, and T. Gao, J. Fluid Mech. **835**, 393 (2018).
[23] A. Opathalage, M. M. Norton, M. P. N. Juniper, B. Langeslay, S. A. Aghvami, S. Fraden, and Z. Dogic, Proc. Natl. Acad. Sci. USA **116**, 4788 (2019).
[24] J. Hardoüin, C. Doré, J. Laurent, T. Lopez-Leon, J. Ignés-Mullol, and F. Sagués, Nat. Commun. **13**, 6675 (2022).
[25] E. de Oliveira, L. Mirantsev, M. Lyra, and I. de Oliveira, J. Mol. Liq. **377**, 121513 (2023).
[26] C. Joshi, Z. Zarei, M. M. Norton, S. Fraden, A. Baskaran, and M. F. Hagan, Soft Matter **19**, 5630 (2023).
[27] W. Luo, A. Baskaran, R. A. Pelcovits, and T. R. Powers, Soft Matter **20**, 738 (2024).
[28] K.-T. Wu, J. B. Hishamunda, D. T. Chen, S. J. DeCamp, Y.-W. Chang, A. Fernández-Nieves, S. Fraden, and Z. Dogic, Science **355**, eaal1979 (2017).
[29] E. Lushi, H. Wioland, and R. E. Goldstein, Proc. Natl. Acad. Sci. USA **111**, 9733 (2014).
[30] S. S. Turzi, Phys. Rev. E **94**, 062705 (2016).
[31] C. M. Bender and S. A. Orszag, *Advanced Mathematical Methods for Scientists and Engineers I: Asymptotic Methods and Perturbation Theory* (Springer Science & Business Media, New York, 1999).